INTERNATIONAL JOURNAL FOR NUMERICAL METHODS IN FLUIDS
Int. J. Numer. Meth. Fluids 2004; **46**:1201–1210
Published online 6 October 2004 in Wiley InterScience (www.interscience.wiley.com). DOI: 10.1002/fld.796

Performance analysis of ventricular assist devices using finite element flow simulation

M. Behr[1,2,*,†], D. Arora[2], Y. Nosé[3] and T. Motomura[3]

[1]*Chair for Computational Analysis of Technical Systems, RWTH Aachen, Steinbachstr. 53B, 52074 Aachen, Germany*
[2]*Mechanical Engineering and Material Science, Rice University, MS 321, 6100 Main St, Houston, TX 77005, U.S.A.*
[3]*DeBakey Department of Surgery, Baylor College of Medicine, 1 Baylor Plaza, Houston, TX 77030, U.S.A.*

SUMMARY

Numerical simulation plays an increasingly important role in the design of medical devices in general, and ventricular assist devices in particular. Modelling of flow in blood pumps has the potential to shorten the design cycle and give the designers important insights into causes of blood damage and suboptimal performance. We present a set of flow simulations designed to reproduce previously obtained experimental data relating flow volume generated by the pump to the pressure head imposed between the outflow and inflow cannulas. These performance curves are obtained using a stabilized space–time finite element formulation of the Navier–Stokes equations, with a shear-slip mesh update used to accommodate the movement of the impeller with respect to non-axisymmetric housing. Copyright © 2004 John Wiley & Sons, Ltd.

KEY WORDS: VAD design; pump performance; blood flow simulation; finite element method

1. INTRODUCTION

Numerical modelling plays an increasingly important role in the design of medical devices. Ventricular assist devices (VADs) in particular can benefit from fluid flow analysis in their interior. These blood pumps are often the last hope of heart disease patients, due to a drastic and chronic shortage of donor hearts available for transplantation. Incorporation of computational analysis into the design process of VADs is critical in order to improve their efficiency and biocompatibility, while maintaining the small size that allows implantation.

While the development of continuous-flow blood pumps dates back to almost 45 years ago, they have been seriously considered as an alternative to pulsatile devices only during the

*Correspondence to: M. Behr, Chair for Computational Analysis of Technical Systems, RWTH Aachen, Steinbachstr. 53B, 52074 Aachen, Germany.
†E-mail: behr@cats.rwth-aachen.de

Contract/grant sponsor: National Science Foundation; contract/grant number: CTS-ITR-0312764
Contract/grant sponsor: NEDO (New Energy and Industrial Technology Development Organization)

Received 3 June 2003
Revised 17 May 2004

last two decades. Their main advantage is simplicity and reliability; they typically have only a single moving part (the impeller), driven via a magnetic coupling. Rotary blood pumps have rapidly progressed from 2-day models for bypass applications, through 2-week pumps for short-term circulatory assistance, to 2-year bridge to transplant [1]. They are now on the verge of being accepted as a permanent clinical solution to heart dysfunction. Various types of rotary blood pump have been proposed. Centrifugal vane-less pumps, e.g. Medtronic Bio-Pump, accelerate the fluid by means of rotating concentric cones. Axial pumps, such as the DeBakey/NASA pump [2], propel the fluid using a miniature turbine, with an axis parallel to the flow direction. Centrifugal pumps, such as the Baylor/Kyocera KP and Baylor PI series [3], use pressure variations produced by rotating vanes to drive the fluid from a central inlet towards the peripheral outlet. While the centrifugal pumps are larger than the axial pumps, their rotational speed is typically lower, leading to 'gentler' flow fields and more physiological conditions.

Computational fluid dynamics (CFD) clearly constitutes an important tool for blood pump design. Even with rapid prototyping capabilities, the experimental studies are constrained by cost and time limitations, and do not generally allow for looking at a large number of alternative designs. Some pumps that were modelled numerically are Utah–Virginia CFVAD3 [4], Impella Intracardiac Pump [5], Nikkiso HPM [6], Aries Isoflow [7] and others. In the case of Pittsburgh Streamliner [8, 9], the modelling was used to *optimize* the shape of certain axial pump components, based on numerically computed flow field. Mathematical models are being developed in order to accurately predict blood damage (index of hemolysis) in the pumps solely on the basis of computational flow analysis [10].

Our approach to blood flow modelling in deforming domain is based on the deformable-spatial-domain/stabilized space–time (DSD/SST) finite element formulation [11, 12]. In space–time methods, the stabilized finite element formulations of the governing equations are written over the space–time domain of the problem. Consequently, changes in the shape of the spatial domain due to the motion of the boundaries and interfaces are taken into account automatically. The initial application of this method to blood flow simulation [13] is now followed by an extensive set of simulations designed to validate this approach against the available experimental data.

In Section 2, we briefly review the governing equations and their stabilized finite element formulation. In Section 3, we describe the experimental set-up that will serve to validate some of our numerical results. In Section 4, we focus on the definition and implementation of the boundary conditions compatible with the experiment. In Section 5, we compare the results of computations with the previously obtained experimental data. We end with concluding remarks in Section 6.

2. GOVERNING EQUATIONS AND DISCRETIZATION

We consider a viscous, incompressible fluid occupying a time-varying domain $\Omega_t \subset \mathbb{R}^{n_{\text{sd}}}$, with boundary Γ_t, where n_{sd} is the number of space dimensions. Velocity $\mathbf{u}(\mathbf{x}, t)$ and pressure $p(\mathbf{x}, t)$ fields are governed by the incompressible Navier–Stokes equations:

$$\rho(\mathbf{u}_{,t} + \mathbf{u} \cdot \nabla \mathbf{u} - \mathbf{f}) - \nabla \cdot \boldsymbol{\sigma}(\mathbf{u}, p) = \mathbf{0} \quad \text{on } \Omega_t \tag{1}$$

$$\nabla \cdot \mathbf{u} = 0 \quad \text{on } \Omega_t \tag{2}$$

where $\mathbf{f}$ is the body force such as gravity, and the density ρ is assumed to be constant. For a Newtonian fluid, stress tensor $\boldsymbol{\sigma}$ is:

$$\boldsymbol{\sigma}(\mathbf{u}, p) = -p\mathbf{I} + 2\mu\boldsymbol{\varepsilon}(\mathbf{u}), \quad \boldsymbol{\varepsilon}(\mathbf{u}) = \frac{1}{2}(\nabla\mathbf{u} + (\nabla\mathbf{u})^{\mathrm{T}}) \tag{3}$$

where μ is the dynamic viscosity. The Dirichlet and Neumann-type boundary conditions are:

$$\mathbf{u} = \mathbf{g} \quad \text{on } (\Gamma_t)_{\mathbf{g}} \tag{4}$$

$$\mathbf{n}\cdot\boldsymbol{\sigma}(\mathbf{u}, p) = \mathbf{h} \quad \text{on } (\Gamma_t)_{\mathbf{h}} \tag{5}$$

where $(\Gamma_t)_{\mathbf{g}}$ and $(\Gamma_t)_{\mathbf{h}}$ are complementary subsets of the boundary Γ_t.

The finite element function spaces for the space–time method are based on the partition of the time interval $(0, T)$ into subintervals $I_n = (t_n, t_{n+1})$, where t_n and t_{n+1} belong to an ordered series of time levels $0 = t_0 < t_1 < \cdots < t_N = T$. Let $\Omega_n = \Omega_{t_n}$ and $\Gamma_n = \Gamma_{t_n}$. We define the space–time slab Q_n as the domain enclosed by the surfaces Ω_n, Ω_{n+1}, and P_n, where P_n is the surface described by the boundary Γ_t as t traverses I_n. As it is the case with Γ_t, surface P_n is decomposed into $(P_n)_{\mathbf{g}}$ and $(P_n)_{\mathbf{h}}$ with respect to the type of boundary condition (Dirichlet and Neumann) being applied.

After introducing suitable trial solution spaces for the velocity and pressure [14], $(\mathscr{S}_{\mathbf{u}}^h)_n$ and $(\mathscr{S}_p^h)_n$, and test function spaces, $(\mathscr{V}_{\mathbf{u}}^h)_n$ and $(\mathscr{V}_p^h)_n$, the stabilized space–time formulation of Equations (1) and (2) is written as follows: given $(\mathbf{u}^h)_n^-$, find $\mathbf{u}^h \in (\mathscr{S}_{\mathbf{u}}^h)_n$ and $p^h \in (\mathscr{S}_p^h)_n$ such that $\forall \mathbf{w}^h \in (\mathscr{V}_{\mathbf{u}}^h)_n$ and $\forall q^h \in (\mathscr{V}_p^h)_n$:

$$\begin{aligned}
&\rho(\mathbf{w}^h, \mathbf{u}_{,t}^h + \mathbf{u}^h\cdot\nabla\mathbf{u}^h - \mathbf{f}^h)_{Q_n} + (\boldsymbol{\varepsilon}(\mathbf{w}^h), \boldsymbol{\sigma}(\mathbf{u}^h, p^h))_{Q_n} \\
&\quad + (q^h, \nabla\cdot\mathbf{u}^h)_{Q_n} + \rho((\mathbf{w}^h)_n^+, (\mathbf{u}^h)_n^+ - (\mathbf{u}^h)_n^-)_{\Omega_n} \\
&\quad + \sum_{e=1}^{(n_{\mathrm{el}})_n} \frac{\tau}{\rho}(\rho(\mathbf{w}_{,t}^h + \mathbf{u}^h\cdot\nabla\mathbf{w}^h) - \nabla\cdot\boldsymbol{\sigma}(\mathbf{w}^h, q^h), \\
&\qquad \rho(\mathbf{u}_{,t}^h + \mathbf{u}^h\cdot\nabla\mathbf{u}^h - \mathbf{f}^h) - \nabla\cdot\boldsymbol{\sigma}(\mathbf{u}^h, p^h))_{Q_n^e} = (\mathbf{w}^h, \mathbf{h}^h)_{(P_n)_{\mathbf{h}}}
\end{aligned} \tag{6}$$

where $(\cdot, \cdot)_{\square}$ are the appropriate scalar or vector function inner products over domain $\square$ and $(\mathbf{u}^h)_n^{\pm} = \lim_{\varepsilon\to 0} \mathbf{u}(t_n \pm \varepsilon)$. In most applications of our method, both velocity and pressure fields are represented using piecewise linear continuous interpolation functions. More details about our approach, including the stabilization parameters, shear-slip mesh update for handling of rotating domain boundaries, as well as other implementation aspects can be found in Reference [13].

3. EXPERIMENTAL APPARATUS

The flow characteristics, or hydraulic performance, of the GYRO pump being developed at the Baylor College of Medicine are evaluated experimentally using 37% glycerin water. Closed test circuit shown in Figure 1 is composed of test blood pump, reservoir bag, pressure lines,

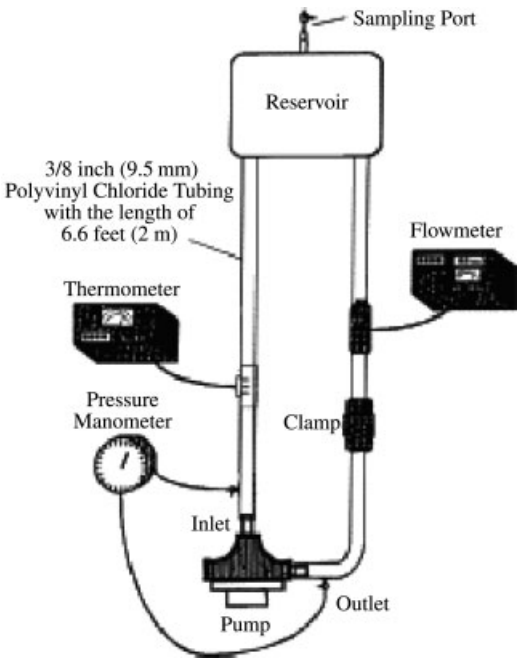

Figure 1. Experimental apparatus.

flow meter, and polyvinyl chloride tube $\frac{3}{8}$ in (9.5 mm) in diameter, and 6.6 ft (2 m) in length. Flow-pressure curves are obtained by driving the impeller at a fixed revolution-per-minute (rpm) rate, and reading the flow meter as well as the pressure drop between the inflow and the outflow tubes. The outflow tube is enclosed in an adjustable clamp, which is then tightened to increase the pressure drop, and consequently reduce the flow. Between 5 and 8 measurements of this type are taken at each rpm rate, from fully open clamp (highest flow) to fully closed clamp (zero flow). Sets of readings are typically taken between 1200 and 2600 rpm, in 200 rpm increments. In Section 5, we compare the sets of readings at 1800, 2000 and 2200 rpm to computational results.

4. BOUNDARY AND INITIAL CONDITIONS

The experimental apparatus described in the previous section is used to obtain hydraulic performance curves (flow versus pressure head at a given rotation speed), and we wish to reproduce similar measurements in a computational setting. Clearly, full computational analysis of the circuit that supports the pump, i.e. tubes, clamps or reservoirs, is to be avoided. We would like to restrict the detailed flow analysis only to the computational domain shown in Figure 2(a), which encompasses the chamber of the GYRO pump, impeller with six top and two bottom vanes, and short sections of the inflow and outflow tubes. The remaining circuit can be either represented as a simplified one-dimensional model with varying flow resistance, or, as is the case here, by imposing a pressure difference across the inflow and outflow boundaries Γ_{in} and Γ_{out}. These boundaries coincide with cross-sections of the inflow and

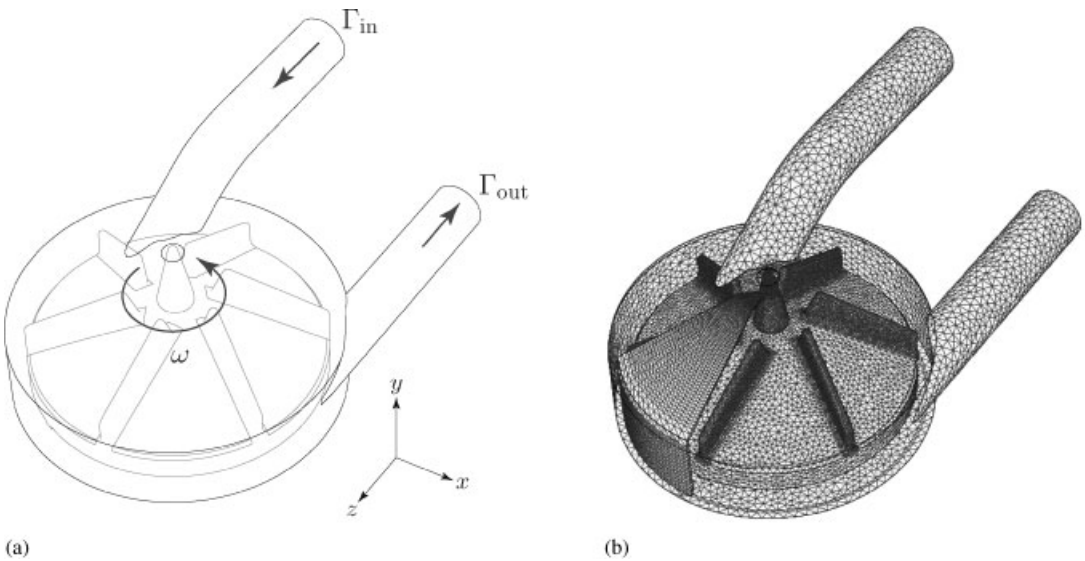

Figure 2. Computational domain and mesh for GYRO rotary blood pump. (a) Domain; and (b) mesh.

outflow tubes. Since the fluid velocity at the inflow and outflow boundary is not determined *a priori*, the boundary conditions on velocity allow arbitrary velocity components along the axes of the inflow and outflow tubes, while the remaining two components are set to zero, thus imposing a parallel flow with arbitrary profile. In order to impose a pressure gradient, we employ a non-homogeneous form of the Neumann boundary condition, evaluating the contributions to the boundary integral in (6) using:

$$\begin{aligned} \mathbf{h}^h \cdot \mathbf{n} &= 0 \quad \text{on } \Gamma_{\text{in}} \\ \mathbf{h}^h \cdot \mathbf{n} &= \Delta p \quad \text{on } \Gamma_{\text{out}} \end{aligned} \tag{7}$$

where Δp is the prescribed pressure head and $\mathbf{n}$ is a unit surface normal vector.

Another implementation issue in these simulations concerns the initial conditions. The use of iterative solution techniques, necessitated by the non-linear nature of the flow problem, as well as by the large size of the coupled equation system involved, requires special care in selecting the initial state of the fluid for a time-dependent simulation. When a good initial flow condition, compatible with the impeller rotating at full velocity, is not available, the impeller angular velocity ω is ramped linearly from zero to the desired value, e.g. 1800 rpm, over the course of a number of time steps. Subsequently, the pressure head Δp was ramped from zero to the desired value, e.g. 100 mm Hg (13.332 kPa) over a similar period. The simultaneous ramping of both the angular velocity and pressure head is avoided in order to prevent flow reversal.

5. HYDRAULIC PERFORMANCE

The test problem, corresponding to the experiment described in Section 3, is a three-dimensional model of the GYRO pump. The geometry shown in Figure 2(a) is similar to

the one in References [13, 15], with evolutionary changes in the impeller shape and inflow tube design. The fluid domain being analysed is bounded by the circular pump housing with diameter of 2.20 in (56.4 mm), conical top and bottom lids, and inflow and outflow tubes with diameter of 0.42 in (10.7 mm). Inside the housing spins an impeller with six top and two bottom vanes. Selected surfaces of the fluid domain, and their finite element discretization, are shown in Figure 5. The finite element mesh consists of 1 138 145 tetrahedral space–time elements and 393 786 space–time nodes. The shear-slip [13] portion of the mesh contains 58 200 tetrahedral elements in a structured one-element-thick layer that forms an inverted "pot" enclosing the impeller; a 45° section of that layer is also shown in Figure 5. The shear-slip layer accommodates the rotation of the impeller and surrounding mesh with respect to the housing by deforming and regenerating as frequently as once per time step. The fluid is assumed to be Newtonian, with a constant viscosity of 3.354 cP, and a density of 1 g/cm^3, corresponding to the glycerin solution used in the experiment.

We focus on reproducing three performance curves available from the experiment, at the impeller angular velocity of 2200, 2000 and 1800 rpm. The simulations are performed for various pressure head values, and they continue as long as it takes for the flow to stabilize, as determined by the time history of the flux through the outflow boundary Γ_{out}. We use Newton–Raphson iterative scheme with 4–8 non-linear iterations, and a diagonally scaled GMRES iterative solver with Krylov space size of 80 and 1 restart. Computations are performed on a Linux PC cluster, with Myrinet interconnect, on partitions ranging from 32 to 72 CPUs.

5.1. *Simulations at* 2200 *rpm*

The time step used was $\Delta t = 0.000272$ s resulting in 100 steps per revolution. For the first run at $\Delta p = 100$ mm Hg, the angular velocity of the impeller was ramped linearly over the first 25 steps, left to settle for the next 25 steps, and then the pressure head ramped linearly over the subsequent 25 steps. For other runs, the pressure head was adjusted linearly from previous run over the first 50 steps. The simulations were performed at $\Delta p = 100$, 110, 120 and 125 mm Hg for 800, 800, 1200 and 1000 time steps, respectively. The resulting flux through the outflow boundary Γ_{out} for this sequence of four simulations is shown in Figure 3. Flow reversal was observed at $\Delta p = 130$ mm Hg.

5.2. *Simulations at* 2000 *rpm*

The time step used was $\Delta t = 0.000300$ s resulting again in 100 steps per revolution. For the first run at $\Delta p = 80$ mm Hg, the angular velocity of the impeller was ramped linearly over the first 25 steps, left to settle for the next 25 steps, and then the pressure head ramped linearly over the subsequent 25 steps. For other runs, the pressure head was adjusted linearly from previous run over the first 50 steps. The simulations were performed at $\Delta p = 80$, 85, 90, 95, 100 and 105 mm Hg for 800, 800, 700, 600, 1000 and 1000 time steps, respectively. The resulting flux through the outflow boundary Γ_{out} is shown in Figure 4. The flow is nearly stagnant at $\Delta p = 105$ mm Hg.

5.3. *Simulations at* 1800 *rpm*

The time step used was $\Delta t = 0.000333$ s resulting once more in 100 steps per revolution. For the first run at $\Delta p = 70$ mm Hg, the angular velocity of the impeller was ramped linearly over

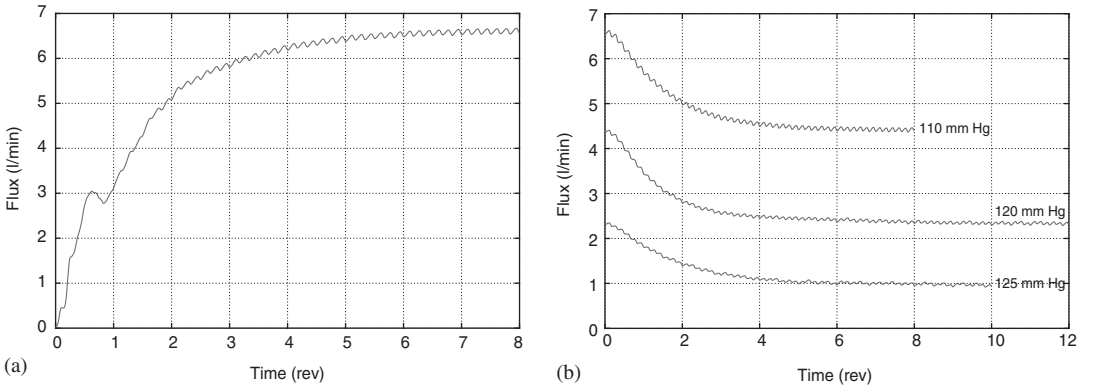

Figure 3. Flux histories at Γ_{out} at $\omega = 2200$ rpm and $\Delta p = 100$, 110, 120 and 125 mm Hg. (a) $\Delta p = 100$ mm Hg; and (b) $\Delta p = 110$–125 mm Hg.

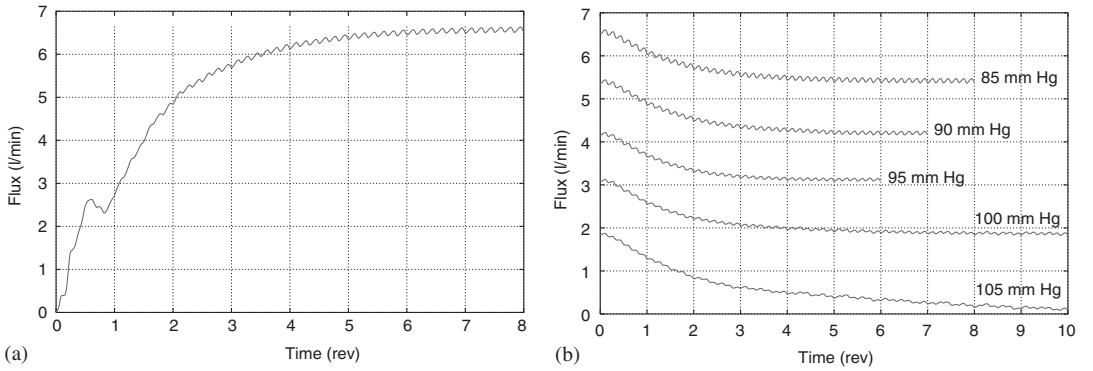

Figure 4. Flux histories at Γ_{out} at $\omega = 2000$ rpm and $\Delta p = 80$, 85, 90, 95, 100 and 105 mm Hg. (a) $\Delta p = 80$ mm Hg; and (b) $\Delta p = 85$–105 mm Hg.

the first 25 steps, left to settle for the next 25 steps, and then the pressure head ramped linearly over the subsequent 25 steps. For other runs, the pressure head was adjusted linearly from previous run over the first 50 steps. The simulations were performed at $\Delta p = 70$, 75, 80 and 85 mm Hg for 1000, 600, 1000 and 1200 time steps, respectively. The resulting flux through the outflow boundary Γ_{out} is shown in Figure 5. The flow is nearly stagnant at $\Delta p = 85$mm Hg.

5.4. Summary of all simulations

The flux histories shown in Figures 3–5 stabilize after 6–12 revolutions of the impeller, in the sense of achieving a sinusoidal profile with constant average and amplitude. The small-scale variations in the flux are due to the six vanes passing the non-axisymmetric features in the housing. In Table I, we show the range of flux values for all simulations, and these are plotted in Figure 6, along with the experimental performance curves.

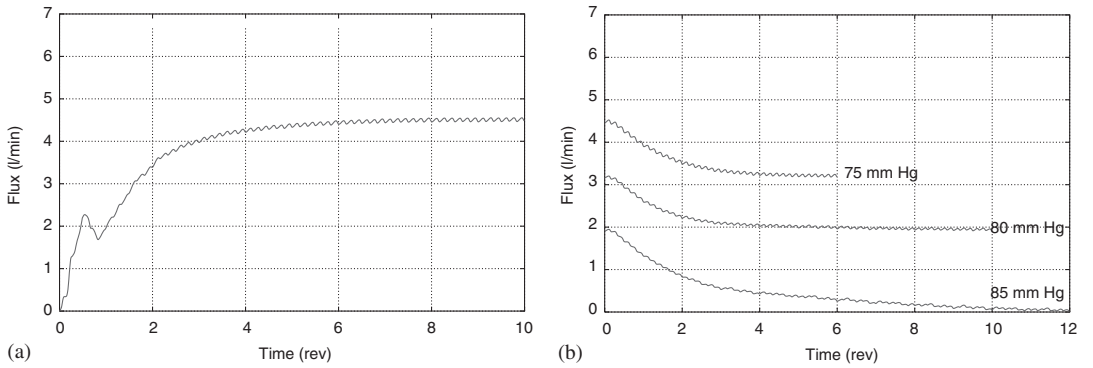

Figure 5. Flux histories at Γ_{out} at $\omega = 1800$ rpm and $\Delta p = 70$, 75, 80 and 85 mm Hg. (a) $\Delta p = 70$ mm Hg; and (b) $\Delta p = 75$–85 mm Hg.

Table I. Minimum and maximum flux through Γ_{out} for a fully developed flow.

Δp (mm Hg)	Q_{min}–Q_{max} (l/min) at 2200 rpm	Q_{min}–Q_{max} (l/min) at 2000 rpm	Q_{min}–Q_{max} (l/min) at 1800 rpm
70			4.541–4.631
75			3.235–3.298
80		6.619–6.747	1.954–2.010
85		5.456–5.564	0.010–0.055
90		4.231–4.317	
95		3.144–3.201	
100	6.653–6.785	1.856–1.918	
105	—	0.083–0.138	
110	4.442–4.540		
120	2.333–2.418		
125	0.933–1.022		

It can be seen that, for angular velocities of 1800 and 2000 rpm, the experimental and computed curves are in close agreement; however, at 2200 rpm, there is a significant difference between the experiment and the computational model. This may be due to the limitation of the Smagorinsky turbulence model used here (with constant $C_s = 0.05$) at the higher rotation rate, and consequently, higher Reynolds number. The influence of the constitutive model should also be investigated; the constant-viscosity model used here should be compared to shear-thinning quasi-Newtonian models, which more accurately reflect the behaviour of both blood and glycerine water solution. Nevertheless, the satisfactory agreement at lower angular speeds is an indication that the computational analysis can be now used in the design phase to conduct preliminary studies of pump performance. As an additional benefit, the computational model has the potential to reliably predict blood damage in the pump, as well as guide the VAD designers towards optimal shape of pump components.

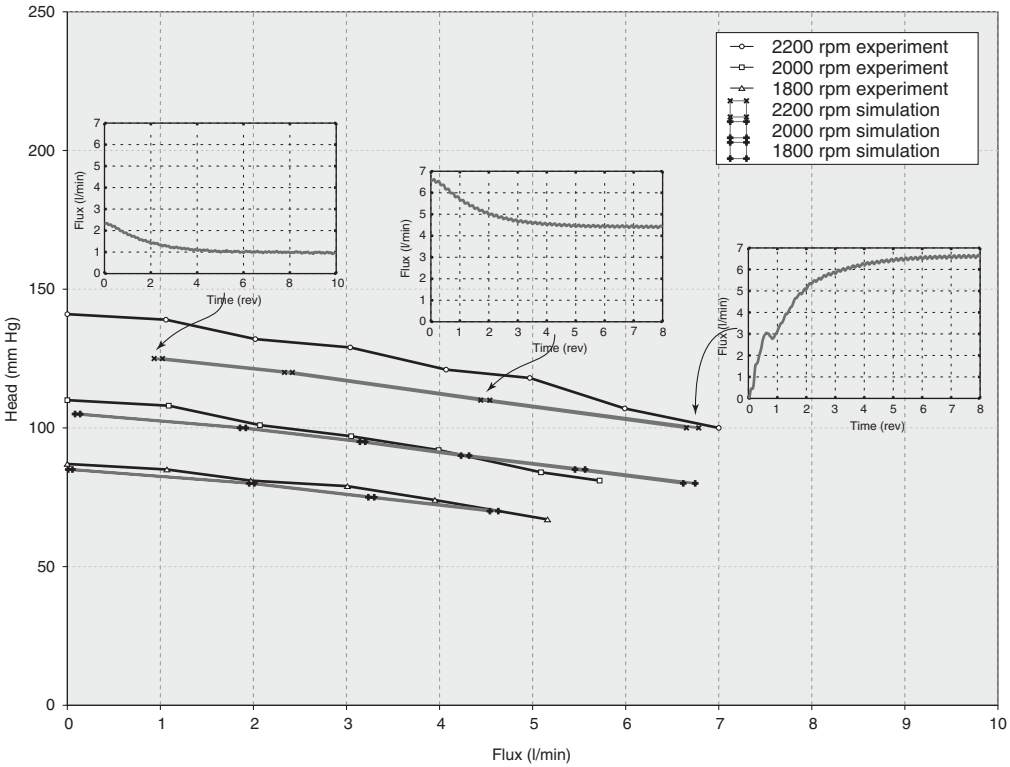

Figure 6. Hydraulic performance: experiment (black) versus simulation (shaded). Some of the previously shown time histories of the flux are also shown.

6. CONCLUDING REMARKS

The set of finite element flow simulations presented here, and their comparison with available experimental data, indicate that computational prediction of ventricular assist device characteristics is possible and viable. In particular, the simulations have reproduced a set of performance curves, relating the flow volume generated at a given angular velocity of the pump impeller to the pressure head imposed across the inlet and the outlet. The agreement was found to be satisfactory, in particular in the lower range of angular velocities, possibly due to the reduced importance of turbulence effects.

ACKNOWLEDGEMENTS

The authors gratefully acknowledge the computing resources made available by the National Partnership for Advanced Computational Infrastructure (NPACI). Additional computing resources were provided by the NSF MRI award EIA-0116289. This work was partially supported by the National Science Foundation under award CTS-ITR-0312764. The pump development programme is supported by NEDO (New Energy and Industrial Technology Development Organization) of Japan.

REFERENCES

1. Nosé Y, Yoshikawa M, Murabayashi S, Takano T. Development of rotary blood pump technology: past, present, and future. *Artificial Organs* 2000; **24**:412–420.
2. Wernicke JT, Meier D, Mizuguchi K, Damm G, Aber G, Denkowski R, Nosé Y, Noon GP, DeBakey ME. A fluid dynamic analysis using flow visualization of the Baylor/NASA implantable axial flow blood pump for design improvement. *Artificial Organs* 1995; **19**:161–177.
3. Yoshikawa M, Nonaka K, Linneweber J, Kawahito S, Ohtsuka G, Nakata K, Takano T, Schulte-Eistrup S, Glueck J, Schima H, Wolner E, Nosé Y. Development of the NEDO implantable ventricular assist device with gyro centrifugal pump. *Artificial Organs* 2000; **24**:459–467.
4. Anderson JB, Wood HG, Allaire PE, Bearnson G, Khanwilkar P. Computational flow study of the continuous flow ventricular assist device, prototype number 3 blood pump. *Artificial Organs* 2000; **24**:377–385.
5. Apel J, Paul R, Klaus S, Siess T, Reul H. Assessment of hemolysis related quantities in a microaxial blood pump by computational fluid dynamics. *Artificial Organs* 2001; **25**:341–347.
6. Miyazoe Y, Sawairi T, Ito K, Konishi Y, Yamane T, Nishida M, Asztalos B, Masuzawa T, Tsukiya T, Endo S, Taenaka Y. Computational fluid dynamics analysis to establish the design process of a centrifugal blood pump: second report. *Artificial Organs* 1999; **23**:762–768.
7. Bludszuweit C. Three-dimensional numerical prediction of stress loading of blood particles in a centrifugal pump. *Artificial Organs* 1995; **19**:590–596.
8. Antaki JF, Ghattas O, Burgreen GW, He B. Computational flow optimization of rotary blood pump components. *Artificial Organs* 1995; **19**:608–615.
9. Burgreen GW, Antaki JF, Wu ZJ, Holmes AJ. Computational fluid dynamics as a development tool for rotary blood pumps. *Artificial Organs* 2001; **25**:336–340.
10. Arora D, Behr M, Pasquali M. Blood damage measures for ventricular assist device modeling. In *Proceedings of the 7th International Conference on Computational Modelling of Free and Moving Boundary Problems*, Mammoli AA (ed.). Wessex Institute of Technology Press: Ashhurst, England, 2003.
11. Tezduyar TE, Behr M, Liou J. A new strategy for finite element computations involving moving boundaries and interfaces—the deforming-spatial-domain/space–time procedure: I. The concept and the preliminary tests. *Computer Methods in Applied Mechanics and Engineering* 1992; **94**:339–351.
12. Tezduyar TE, Behr M, Mittal S, Liou J. A new strategy for finite element computations involving moving boundaries and interfaces—the deforming-spatial-domain/space–time procedure: II. Computation of free-surface flows, two-liquid flows, and flows with drifting cylinders. *Computer Methods in Applied Mechanics and Engineering* 1992; **94**:353–371.
13. Behr M, Arora D. Shear-slip mesh update method: implementation and applications. *Computer Methods in Biomechanics and Biomedical Engineering* 2003; **6**:113–123.
14. Behr M, Tezduyar TE. Finite element solution strategies for large-scale flow simulations. *Computer Methods in Applied Mechanics and Engineering* 1994; **112**:3–24.
15. Behr M. Biofluid simulations on Linux clusters. In *Parallel Computational Fluid Dynamics—New Frontiers and Multi-Disciplinary Applications*, Matsuno K, Ecer A, Periaux J, Satofuka N, Fox P (eds). Elsevier: New York, 2003; 451–458.

